Supplementary Information (SI) for Soft Matter.

Supporting Information: Phase behavior of binary mixtures of hollow and regular microgels

Alexander V. Petrunin,[1,*] Tom Höfken,[1] Stefanie Schneider,[1]
Pablo Mota-Santiago,[2,3] Judith E. Houston,[4] and Andrea Scotti[5,†]

[1] *Institute of Physical Chemistry, RWTH Aachen University, 52056 Aachen, Germany*
[2] *Australian Synchrotron, ANSTO, Clayton, Victoria, Australia*
[3] *MAX IV Laboratory, Lund University, P.O. Box 118, 22100 Lund Sweden*
[4] *European Spallation Source ERIC, Box 176, SE-221 00 Lund, Sweden*
[5] *Division of Physical Chemistry, Lund University, SE-22100 Lund, Sweden*

(Dated: September 27, 2024)

* petrunin@pc.rwth-aachen.de
† andrea.scotti@fkem1.lu.se

S1. SAXS RESULTS FOR BINARY MIXTURES

The position of the first peak in the structure factor, q_{max}, was used to determine the nearest-neighbor distance in the suspension, d_{nn}, according to the relation $d_{nn} = 2.2\pi/q_{max}$ [1–3]. Figure S6 summarizes the obtained d_{nn} values for all studied samples as a function of ζ. In panel (a), the d_{nn} values are plotted for suspensions where fluid-like contribution to $S(q)$ is dominant. The values can be described by the scaling law $d_{nn} \propto \zeta^{-1/3}$ (solid lines in Figure S6(a)). This analytical form typically applies for soft repulsive particles [2–5]. The use of this scaling law highlights a systematic increase of d_{nn} with increasing n_h in the fluid-like suspensions.

The structure factors obtained after equilibrating the samples in sealed capillaries for 1 year are shown in Figure S7. Note that the samples with different n_h were selected at different ζ, roughly in the middle of the coexistence region (Fig. 2(a)), where the crystallization rate is relatively fast compared to $\zeta \simeq \zeta_m$. Notably, the shoulder of the first peak in the $S(q)$, which corresponds to the (200) reflection of the fcc lattice, decreases with increasing n_h. This is related to the increasing stacking disorder of hexagonal planes, so that a transition from predominantly fcc lattice to a rhcp lattice is observed with increasing n_h. The only exception is the sample with $n_h = 0.232$, which has the (200) reflection comparable to the typically most prominent (111) reflection and also shows no (220) reflection. Such atypical diffraction pattern may be explained by a different orientation of crystals inside the SAXS capillary when stacking of hexagonal planes is not parallel to the capillary wall.

S2. UV-VIS ABSORPTION SPECTROSCOPY

UV-Vis absorption spectra in the near-infrared region were recorded for selected binary mixtures to corroborate the SAXS results. The measurements were carried out using the Agilent Cary 60 spectrophotometer at 20°C in the wavelength range from $\lambda = 800$ to 1100 nm with a step of 1 nm. The samples were placed in quartz cells with 1 mm optical path length and equilibrated at 20 °C for at least 2 weeks prior to measurement.

Figure S8(a) shows the UV-Vis absorption spectra of the binary mixtures with different n_h. Similar to SAXS, samples in the middle of the coexistence region were chosen for the measurement because of their higher crystallization rate. The sharp peaks at $\lambda \simeq 1055 - 1060$ nm correspond to the first-order Bragg reflection from the (111) family of planes [6]. The peak shifts slightly to higher wavelength with increasing n_h, while its magnitude decreases dramatically. This is consistent with the inhibition of crystallization that we observed by SAXS.

The lattice constant can be obtained from the peak position following the Bragg's law:

$$2 \cdot n \cdot d_{hkl} \cdot \sin\theta = \lambda \tag{S1}$$

where n is the refractive index of the suspension, $d_{hkl} = a/\sqrt{h^2 + k^2 + l^2}$ is the separation between the (hkl) family of planes, θ is the angle between the planes and incident light, and λ is the wavelength of incident light. Here it is reasonable to assume that all crystals grow from the cell wall ($\sin\theta = 1$), because only one sharp peak is present for every sample [6].

The calculated lattice constants a are plotted in Figure S8(b) with blue circles. We note that the observed peak shift in the spectra (Figure S8(a)) results in only a few nm difference in a. Furthermore, the obtained values are in reasonable agreement with the a-values obtained from SAXS (orange squares) showing only minor changes in the lattice constant with increasing n_h.

S3. DEFORMABILITY OF HOLLOW AND REGULAR MICROGELS FROM CONTINUUM ELASTICITY THEORY

To verify that hollow microgels are more deformable than their regular counterpart, we use a simple continuum mechanics model for a homogeneous elastic capsule. For a capsule of radius R undergoing small uniaxial deformation Δ, the elastic energy is [7]:

$$U_c(\Delta) \propto (G^{1/2}\kappa^{1/2}/R)\Delta^2 \tag{S2}$$

where G is the in-plane elastic modulus (bulk or shear modulus for stretch or shear deformation, respectively) and κ is the bending rigidity.

Considering for simplicity only stretch deformation, one obtains [7]:

$$U_c(\Delta) = \frac{Eh^2}{2R(1-\sigma)\sqrt{6(1+\sigma)}}\Delta^2 \tag{S3}$$

where h is the thickness of the capsule, E is the Young's modulus and σ is the Poisson's ratio of the material.

In contrast, a small deformation of a homogeneous elastic sphere is given by the Hertzian potential [8].

$$U_s(\Delta) = \frac{8}{15} E R^{1/2} \Delta^{5/2} \tag{S4}$$

Now, let us consider a sphere and a hollow capsule of the same radius and the same material ($E_c = E_s$ and $\sigma_c = \sigma_s$). The ratio U_s/U_c then shows how much more deformable a hollow capsule is, solely due to its cavity.

$$\frac{U_s}{U_c} = \frac{16}{15} \frac{(1-\sigma)\sqrt{6(1+\sigma)}}{h^2} \left(\frac{R}{h}\right)^2 \left(\frac{\Delta}{R}\right)^{1/2} \tag{S5}$$

For $h = 0.44R$, which is consistent with our hollow microgels, the ratio U_s/U_c is shown in Fig. S10 (blue circles) as a function of $r = R - \Delta$. The ratio of PMFs obtained from the simulation (orange squares) is also shown for comparison. The elasticity model gives a similar ratio to the simulation result, showing that hollow microgels are 2-4 times easier to deform that regular ones only because of their cavity. We note that the model and the simulation show different dependency on r and only agree qualitatively at $r \approx 0.9$. This fact depends on multiple factors. The first is that at very small deformations the simulation data are not accurate due to poor statistics, whereas at $r > 0.9$ the elasticity model is not applicable because the deformation cannot be considered small. Furthermore, the model has the limitation of not accounting for a fundamental property of soft colloids, the more they are compressed the harder it becomes to compress them further, i.e. their bulk modulus is not constant but increases with compression. Secondly, the simple continuum model completely neglects the polymeric nature of the hollow microgels, in particular the fact that the polymer chains can fold and expand into the cavity cannot be accounted for and can lead to the differences in the ratio. Nonetheless, this simple model already gives a good order-of-magnitude estimate of the high deformability of hollow microgels compared to regular ones, even though it completely ignores their fuzzy structure. Surely the differences reported in Fig. S10 push for a better description of the mechanical properties of the microgels that need to go beyond the classic continuum mechanics of elastic bodies.

S4. SUPPLEMENTARY FIGURES

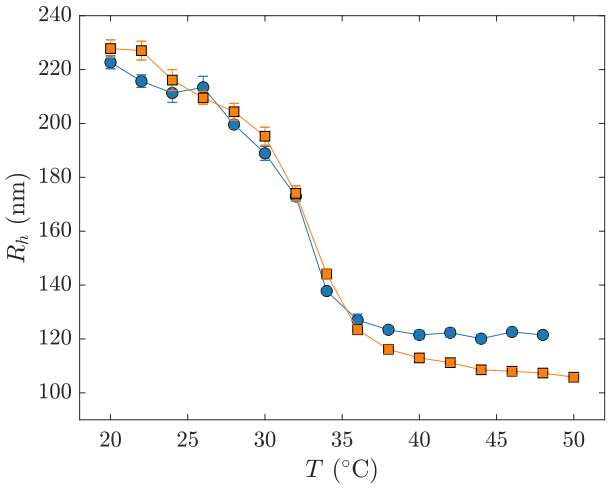

FIG. S1. Hydrodynamic radii R_h of regular microgels (blue circles) and hollow microgels (orange squares) obtained using DLS as a function of temperature.

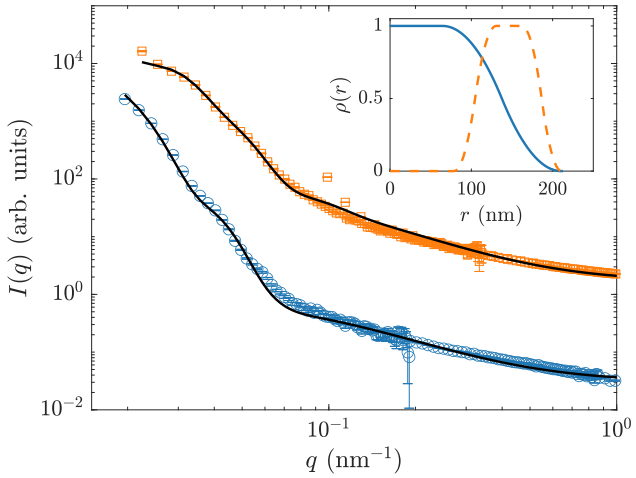

FIG. S2. Form factors of regular microgels (blue circles) and hollow microgels (orange triangles) measured with SANS. Black lines show fits of the data using the fuzzy sphere model or fuzzy core-shell model. The curves are shifted along the y-axis for clarity. Inset: radial distributions of relative polymer volume fraction $\rho(r)$ for regular microgels (blue solid line) and hollow microgels (orange dashed line). The values of $\rho(r)$ are normalized between 0 and 1.

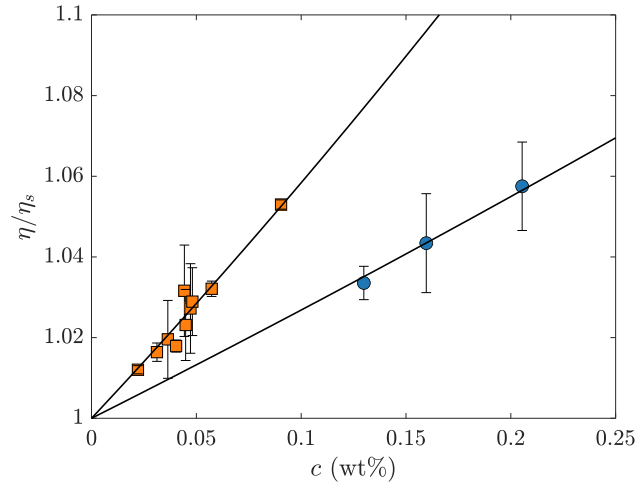

FIG. S3. Relative viscosity η/η_s of suspensions of regular microgels (blue circles) and hollow microgels (orange squares) as a function of weight fraction c. Black solid lines are fits with Equation 1.

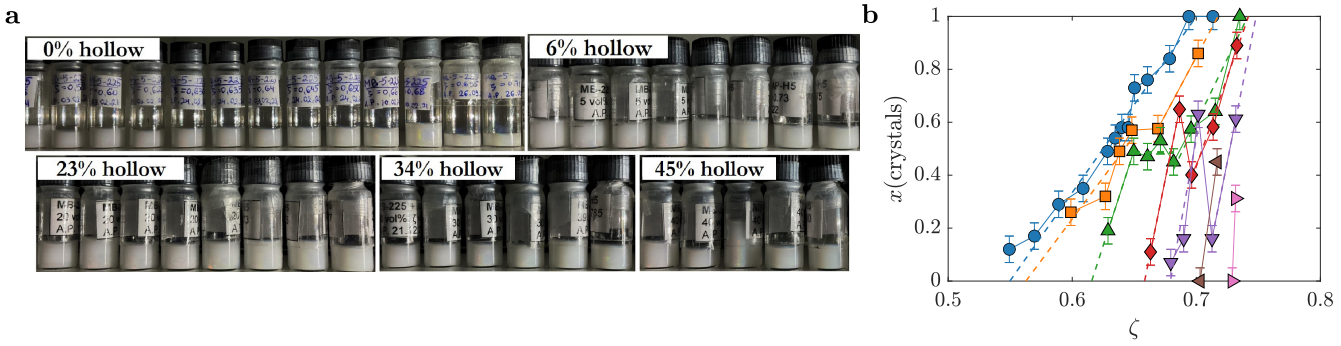

FIG. S4. (a) Photos of the binary mixtures with different contents of hollow microgels. Crystals are visible as bright iridescent spots. (b) Fraction of crystals for the samples in the fluid-crystal coexistence region with $n_h = 0$ (blue circles), $n_h \approx 0.06$ (orange squares), $n_h \approx 0.23$ (green upward triangles), $n_h \approx 0.34$ (red diamonds), $n_h \approx 0.45$ (purple downward triangles), $n_h \approx 0.55$ (brown left triangles), and $n_h \approx 0.64$ (pink right triangles). Dashed lines correspond to linear fits of the data.

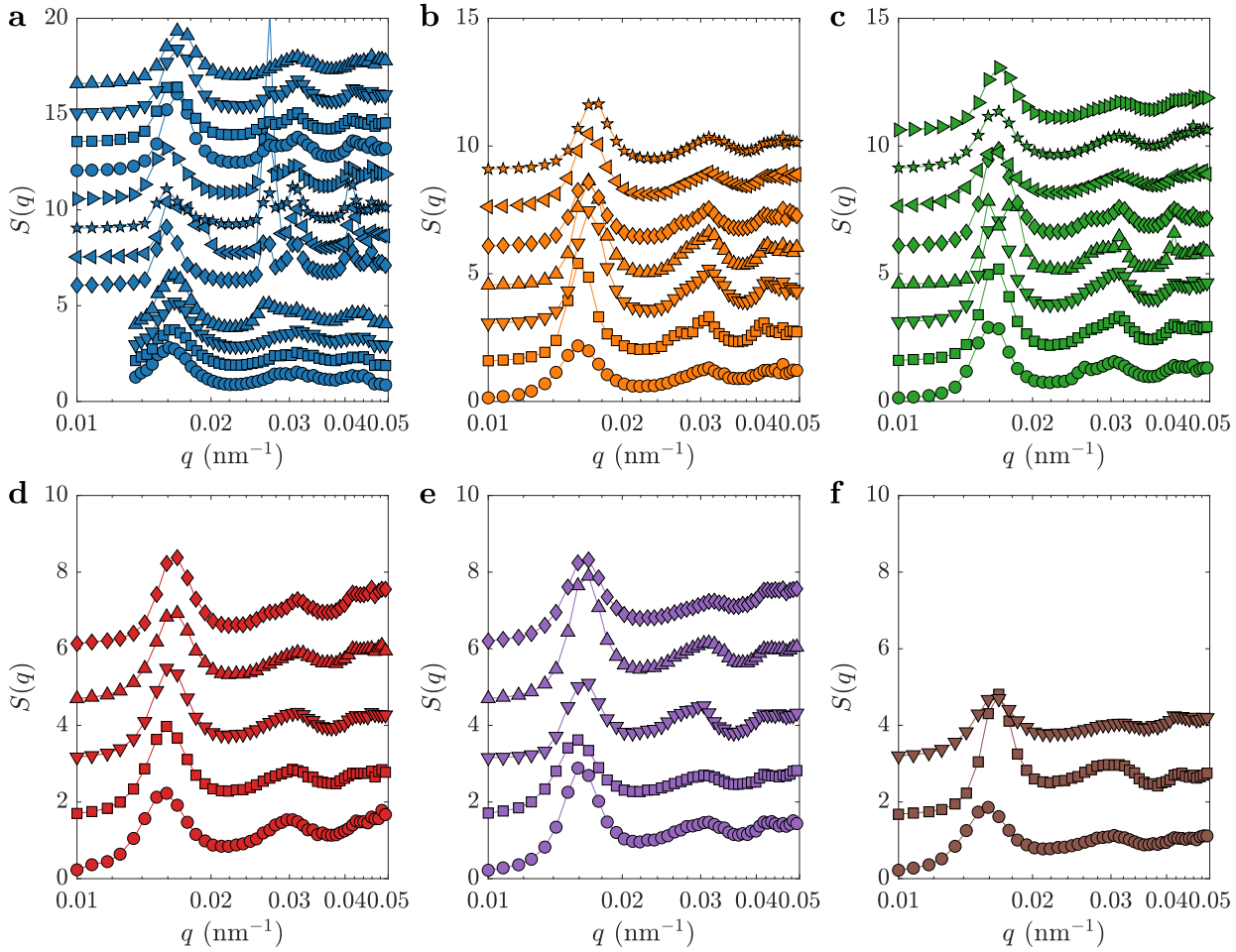

FIG. S5. SAXS structure factors for (a) regular microgels ($n_h = 0$) and ζ (from bottom to top): 0.549 ± 0.006, 0.570 ± 0.006, 0.589 ± 0.007, 0.61 ± 0.01, 0.628 ± 0.005, 0.635 ± 0.005, 0.640 ± 0.002, 0.645 ± 0.005, 0.650 ± 0.005, 0.661 ± 0.005, 0.679 ± 0.005, 0.69 ± 0.01, 0.71 ± 0.01, 0.731 ± 0.002; (b) binary mixtures with $n_h \approx 0.06$ and ζ (from bottom to top): 0.590 ± 0.003, 0.627 ± 0.003, 0.638 ± 0.003, 0.648 ± 0.003, 0.702 ± 0.004, 0.721 ± 0.004, 0.741 ± 0.004; (c) binary mixtures with $n_h \approx 0.23$ and ζ (from bottom to top): 0.63 ± 0.01, 0.65 ± 0.01, 0.66 ± 0.01, 0.67 ± 0.01, 0.68 ± 0.01, 0.70 ± 0.01, 0.72 ± 0.01, 0.74 ± 0.01; (d) binary mixtures with $n_h \approx 0.34$ and ζ (from bottom to top): 0.64 ± 0.02, 0.66 ± 0.02, 0.70 ± 0.02, 0.71 ± 0.02, 0.73 ± 0.02; (e) binary mixtures with $n_h \approx 0.45$ and ζ (from bottom to top): 0.68 ± 0.02, 0.69 ± 0.02, 0.70 ± 0.02, 0.71 ± 0.02, 0.73 ± 0.02; (f) binary mixtures with $n_h \approx 0.55$ and ζ (from bottom to top): 0.70 ± 0.03, 0.72 ± 0.03, 0.73 ± 0.03. The data are shifted along y-axis for clarity.

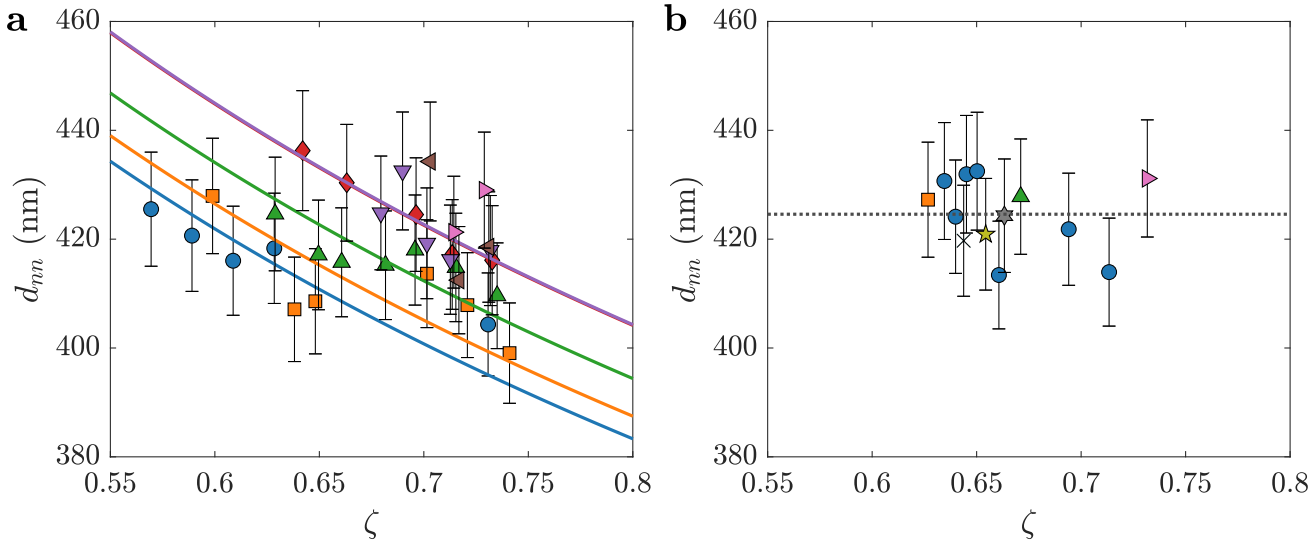

FIG. S6. Average nearest-neighbor distances d_{nn} obtained from SAXS for samples with dominant fluid-like structure factor (a) and samples with dominant crystalline structure factor (b). Marker type corresponds to the content of hollow microgels: $n_h = 0$ (blue circles), $n_h \approx 0.025$ (black crosses), $n_h \approx 0.06$ (orange squares), $n_h \approx 0.12$ (olive pentagrams), $n_h \approx 0.18$ (grey hexagrams), $n_h \approx 0.23$ (green upward triangles), $n_h \approx 0.34$ (red diamonds), $n_h \approx 0.45$ (purple downward triangles), $n_h \approx 0.55$ (brown left triangles), and $n_h \approx 0.64$ (pink right triangles). Solid lines in panel (a) correspond to data fits with the scaling law $d_{nn} \propto \zeta^{-1/3}$. Horizontal dashed line in panel (b) corresponds to the average d_{nn} in samples with dominant crystalline structure factor.

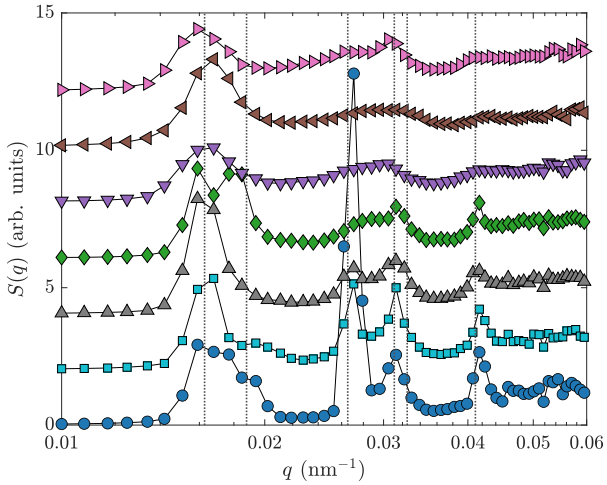

FIG. S7. SAXS structure factors after equilibration for 1 year for binary mixtures with $\zeta = 0.640 \pm 0.002$ and $n_h = 0$ (blue circles), $\zeta = 0.644 \pm 0.002$ and $n_h = 0.025 \pm 0.001$ (cyan squares), $\zeta = 0.663 \pm 0.009$ and $n_h = 0.176 \pm 0.001$ (grey upward triangles), $\zeta = 0.67 \pm 0.01$ and $n_h = 0.232 \pm 0.001$ (green diamonds), $\zeta = 0.70 \pm 0.02$ and $n_h = 0.448 \pm 0.001$ (purple downward triangles), $\zeta = 0.72 \pm 0.03$ and $n_h = 0.548 \pm 0.001$ (brown left triangles), $\zeta = 0.73 \pm 0.03$ and $n_h = 0.645 \pm 0.001$ (pink right triangles). Vertical dotted lines correspond to Bragg reflections of an fcc structure (for the sample with $n_h = 0$).

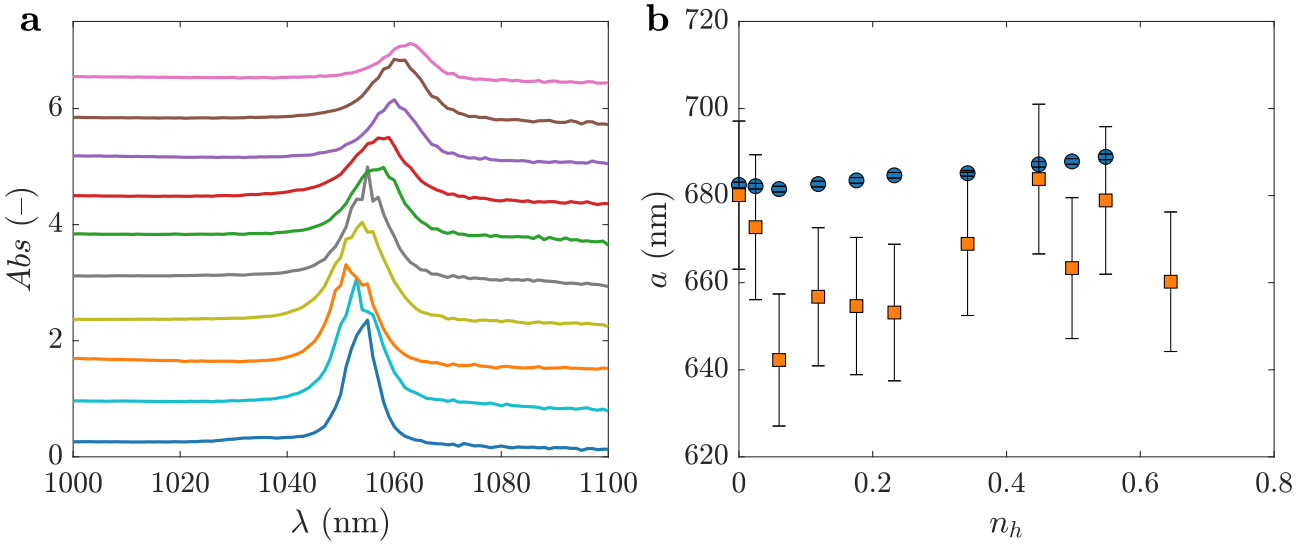

FIG. S8. (a) UV-Vis absorption spectra of the binary mixtures showing Bragg reflections for (from bottom to top): $\zeta = 0.640 \pm 0.002$ and $n_h = 0$, $\zeta = 0.644 \pm 0.002$ and $n_h = 0.025 \pm 0.001$, $\zeta = 0.648 \pm 0.003$ and $n_h = 0.060 \pm 0.001$, $\zeta = 0.654 \pm 0.006$ and $n_h = 0.119 \pm 0.001$, $\zeta = 0.663 \pm 0.009$ and $n_h = 0.176 \pm 0.001$, $\zeta = 0.67 \pm 0.01$ and $n_h = 0.232 \pm 0.001$, $\zeta = 0.69 \pm 0.02$ and $n_h = 0.342 \pm 0.001$, $\zeta = 0.70 \pm 0.02$ and $n_h = 0.448 \pm 0.001$, $\zeta = 0.71 \pm 0.03$ and $n_h = 0.498 \pm 0.001$, $\zeta = 0.72 \pm 0.03$ and $n_h = 0.548 \pm 0.001$. (b) Crystal lattice constant a (assuming an fcc structure) obtained from UV-Vis data (blue circles) and SAXS data (orange triangles) for the same samples shown in panel (a).

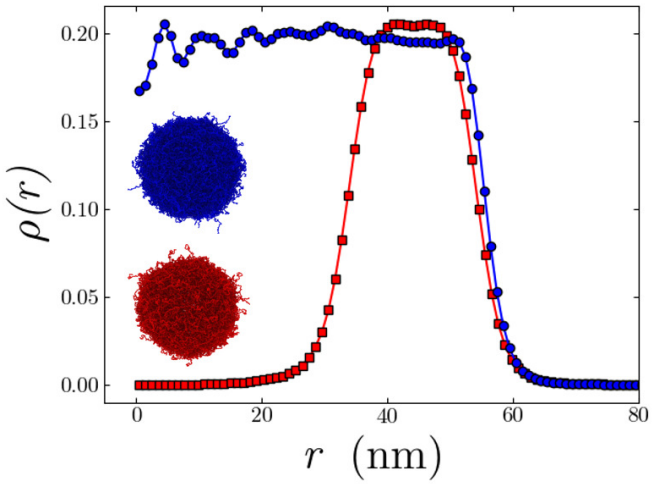

FIG. S9. Radial density profile of the simulated regular (blue circles) and hollow (red squares) microgels. Both microgels have a similar radius, crosslink fraction, network density and fuzziness. They only differ in the central cavity and, therefore, the regular microgel has to consists of 1.5 times more beads.

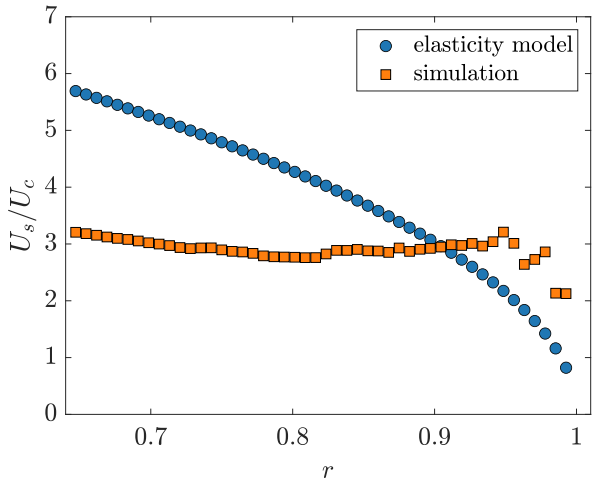

FIG. S10. Ratio of elastic energy for deforming a homogeneous sphere U_s and a homogeneous hollow capsule U_c (blue circles) as a function of distance from the particle center r (in units of R). The corresponding ratio of potentials of mean force for compressing two regular *vs.* two hollow microgels obtained from the simulation is shown for comparison (orange squares).

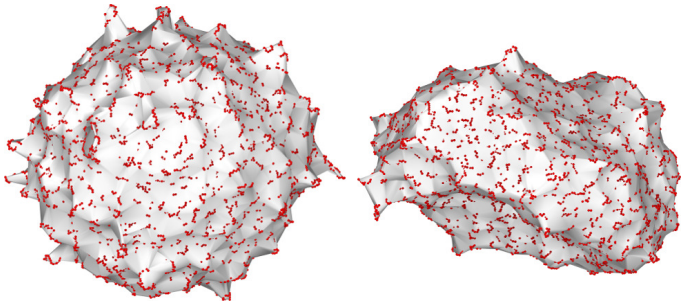

FIG. S11. Surface mesh of a hollow (left) and a deformed hollow (right) microgel used for volume calculations. It is created with the alpha shape algorithm and an alpha parameter of 10 bead diameters.

[1] J. Liu, H.-J. Schöpe, and T. Palberg, Particle & Particle Systems Characterization: Measurement and Description of Particle Properties and Behavior in Powders and Other Disperse Systems **17**, 206 (2000).
[2] P. S. Mohanty, S. Nöjd, K. van Gruijthuijsen, J. J. Crassous, M. Obiols-Rabasa, R. Schweins, A. Stradner, and P. Schurtenberger, Scientific Reports **7**, 1487 (2017).
[3] G. M. Conley, P. Aebischer, S. Nöjd, P. Schurtenberger, and F. Scheffold, Science advances **3**, e1700969 (2017).
[4] A. Scotti, U. Gasser, E. S. Herman, M. Pelaez-Fernandez, J. Han, A. Menzel, L. A. Lyon, and A. Fernández-Nieves, Proceedings of the National Academy of Sciences **113**, 5576 (2016).
[5] A. Scotti, U. Gasser, E. Herman, J. Han, A. Menzel, L. A. Lyon, and A. Fernandez-Nieves, Physical Review E **96**, 032609 (2017).
[6] B. Sierra-Martin and A. Fernandez-Nieves, Soft Matter **8**, 4141 (2012).
[7] F. Dubreuil, N. Elsner, and A. Fery, The European Physical Journal E **12**, 215 (2003).
[8] I. Bouhid de Aguiar, T. Van de Laar, M. Meireles, A. Bouchoux, J. Sprakel, and K. Schroën, Scientific reports **7**, 10223 (2017).